

# Single cell induced optical confinement in biological lasers

M Karl, C P Dietrich, M Schubert, I D W Samuel, G A Turnbull and M C Gather<sup>1</sup>

Organic Semiconductor Centre, SUPA, School of Physics and Astronomy, University of St Andrews, St Andrews KY16 9SS, UK

E-mail: [mcg6@st-andrews.ac.uk](mailto:mcg6@st-andrews.ac.uk)

Received 1 September 2016, revised 28 November 2016

Accepted for publication 13 December 2016

Published 31 January 2017



## Abstract

Biological single cell lasers have shown great potential for fundamental research and next generation sensing applications. In this study, the potential of fluorescent biological cells as refractive index landscapes and active optical elements is investigated using a combined Fourier- and hyperspectral imaging technique. We show that the refractive index contrast between cell and surrounding leads to 3D confinement of photons inside living cells. The Fourier- and real-space emission characteristics of these biological lasers are closely related and can be predicted from one another. Investigations of the lasing threshold for different energy and momentum position in Fourier-space give insight into the fundamental creation of longitudinal and transverse lasing modes within the cell. These findings corroborate the potential of living biological materials for precision engineering of photonic structures and may pave the way towards low threshold polariton lasing from single cells.

Keywords: biolaser, optical confinement, microcavities, Fourier imaging, hyperspectral imaging

(Some figures may appear in colour only in the online journal)

## 1. Introduction

The invention of the laser by Maiman in 1960 [1] made a tremendous impact on our lives and advanced biology and medicine in fundamental research and applications alike. The medical applications of laser light include for example treatment of skin cancer via photodynamic therapy (PDT) [2], cosmetic dermatology via laser surgery [3] and diagnostic imaging of the human eye via scanning laser ophthalmoscopy [4]. Despite the enormous advances these techniques have brought, they rely almost exclusively on delivery of conventionally generated laser light to a specific region within the target tissue. This dogma has recently been challenged by

<sup>1</sup> This article belongs to the [special issue: Emerging Leaders](#), which features invited work from the best early-career researchers working within the scope of *J. Phys. D*. This project is part of the *Journal of Physics series'* 50th anniversary celebrations in 2017. Malte Gather was selected by the Editorial Board of *J. Phys. D* as an emerging Leader.

Original content from this work may be used under the terms of the [Creative Commons Attribution 3.0 licence](#). Any further distribution of this work must maintain attribution to the author(s) and the title of the work, journal citation and DOI.

suggestions to generate stimulated emission in or by biological systems, rather than delivering laser light externally. Such ‘bio-lasers’ may provide valuable information on biological systems by relating the distinct properties of their emission to the characteristics of the biological host material. In 2011 Gather and Yun demonstrated a laser based on a single live cell that produces its own gain medium—the green fluorescent protein (GFP) [5]. While these single cell lasers are unique in terms of size and gain medium, lasing has also been generated in other biological samples such as dye stained animal tissue [6], Vitamin B2 doped gelatine [7], nanoimprinted DNA [8], solid-state fluorescent proteins films [9] and chlorophyll [10].

Single cell lasers can be classified into two categories depending on whether the resonator structure is located outside the cell (extracellular laser) or internalized by the cell (intracellular laser). Intracellular lasers have only been demonstrated very recently and they may find applications in cell tagging and tracking or for intracellular sensing. By measuring the unique spectra of these lasers, it is possible to distinguish individual cells in large cell populations over extended periods of time [11]. It has also been suggested to use them

to monitor intracellular ion concentrations by observing shifts of the lasing spectrum that result from changes in intracellular refractive index [12].

For extracellular lasers, lasing is typically obtained from fluorescent cells in suspension that are located between two highly reflective mirrors forming a Fabry–Pérot microcavity (see figure 1(a)). The gain medium of these lasers can be either a fluorescent protein produced inside the cell, such as GFP [13], or an externally introduced synthetic dye such as 5-chloromethylfluorescein diacetate (CMFDA) [14]. Both types of gain medium form quasi-four level systems in which population inversion can be achieved via nanosecond optical excitation. Lasing occurs above a certain pump pulse threshold which is typically in the nJ-range, orders of magnitude below the onset of photo-induced damage to the cell [5, 14]. The emission spectrum of extracellular lasers consists of multiple narrow-band peaks. Hyperspectral imaging techniques have been used to decompose the near field emission pattern of these lasers into its different spectral components [5]. This allowed identification and assignment of the different peaks as transverse and longitudinal modes. It was also shown that this configuration can be used to study the osmotic pressure of a cell by monitoring the spectral position of the different laser modes [15]. Due to the well-defined directionality of the laser emission, light detection can be more efficient than conventional fluorescence assays for which emission is usually isotropic [16].

Due to the refractive index contrast between the cell and the surrounding medium, the cell acts as a convex lens within the planar Fabry–Pérot cavity of an extracellular laser. This leads to a stable resonator configuration and can accommodate any tilts between the two cavity mirrors which would otherwise destabilize the resonator [15]. Even though lasing from single cells has been observed and studied and first applications have been proposed, the implications of the photonic structure formed by the presence of the cell within the cavity have not yet been investigated in detail and the associated physics are not fully understood.

Microcavities filled with inorganic or organic emitters are widely used to study the interaction of light and matter [17]. (These efforts have to some extent already been mirrored with solid-state films of GFP and other fluorescent proteins which offer unique photophysical properties in terms of concentration and bi-molecular quenching [9]. Such structures facilitate photon lasing [18] and can also provide the basis for room temperature exciton-polariton lasers operating under nanosecond rather than picosecond excitation [19].) Multi-dimensional confinement of electromagnetic fields within microcavities offers a powerful tool to study coherent emission over macroscopic distances and in lasers based on organic materials such studies can be conveniently performed at room temperature [20]. The fundamental strategy of these structures is to introduce lateral discontinuities in refractive index to a layer within the cavity which then leads to optical confinement [21]. So far, these techniques have typically relied on lithographic patterning of a metal or an inorganic dielectric within the cavity. However, an inherent property of the single

cell laser is the refractive index contrast between the cell and the surrounding medium and we hypothesize that this can be harnessed for studying light matter interaction and for trapping photons in a biological system.

In the present study, we utilize combined Fourier- and hyperspectral imaging of single cell lasers to investigate their fundamental photonic properties. We find that the inherent refractive index difference between a cell and the surrounding medium and the presence of the Fabry–Pérot resonator lead to confinement of photons in three dimensions within the cell. By comparing Fourier-space (i.e. angle/momentum resolved) and real-space emission, it is possible to relate the observed transverse mode patterns to different energetic states in Fourier-space. Furthermore, we studied the pump threshold for lasing as a function of momentum and energy in Fourier-space. The observations are compared to two reference structures, either providing synthetic photonic confinement and mimicking the photonic landscape presented by the cell or without any in-plane photonic confinement.

## 2. Materials and methods

### 2.1. Cell culturing, cell staining and cavity fabrication

Cells from the HEK 293 cell line (derived from human embryonic kidney cells, Sigma Aldrich) were cultured in DMEM (Dulbecco's Modified Eagle Medium, Thermo Fisher Scientific) with 10% (v/v) fetal bovine serum (FBS, Thermo Fisher Scientific) and 1% penicillin–streptomycin (Thermo Fisher Scientific) under standard incubation conditions (37 °C, 5% CO<sub>2</sub>) until about 50% confluency.

The dye CMFDA (Life Technologies) was selected for cell staining. CMFDA allows rapid formation of single cell lasers since the fluorescence of this dye is only activated when it interacts with the cytoplasm and this interaction also modifies the dye to become membrane-impermeable (see [14] for details). HEK 293 cells were incubated in CMFDA (concentration, 200  $\mu$ M) for 30 min. Using quantitative fluorescence microscopy, we estimated the final intracellular dye concentration to be 700  $\mu$ M by comparing the relative intensity of the fluorescent cells to a fluorescent reference sample. We attribute this increase in concentration over the original CMFDA staining solution to an intracellular accumulation of non-membrane-permeable dye.

Laser cavities were formed by two highly reflective circular distributed Bragg reflector (DBR) mirrors with 25.4 mm diameter. Each mirror had a photonic stop band with reflectivity  $R > 99\%$  that was centred at 532 nm and ranged from 480 to 590 nm. To obtain a defined cavity length, glass beads with a calibrated diameter of 10  $\mu$ m were gently sprinkled onto the bottom mirror before placing the second mirror on top and gluing the mirrors together using an adhesive polymer (see figure 1(b)). The fluorescent cells were suspended in phosphate buffered saline solution (PBS) to prevent background fluorescence and provide physiological osmolarity and ion concentration. 20  $\mu$ l of cell solution was transferred into the cavity void from the edge of the mirrors via capillary forces.

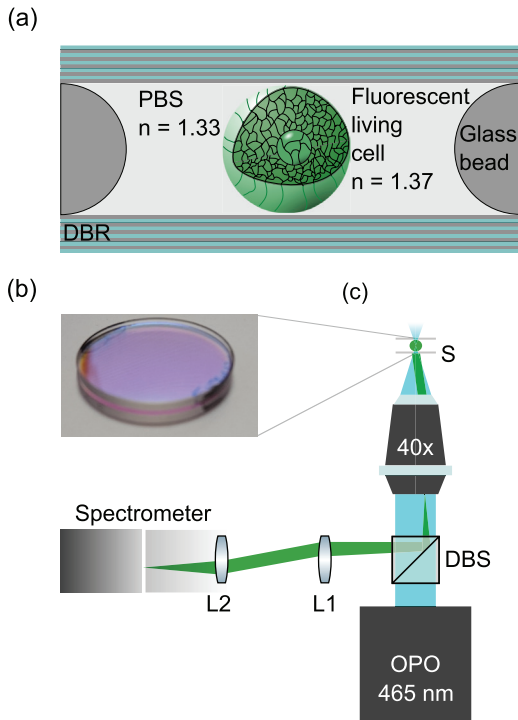


**Figure 1.** Experimental set up. (a) Illustration and (b) picture of the extracellular single cell laser. A fluorescent biological cell suspended in PBS (phosphate buffered saline solution) is embedded between two DBR mirrors which are spaced using glass beads and sealed using a polymer adhesive. (c) Illustration of the optical characterization setup for Fourier-imaging in which *S* denotes the single cell laser sample, DBS is a dichroic beam splitter with an onset at 500 nm, L1 is a lens collecting emission from the back focal plane of the 40 $\times$  objective and L2 is a projection lens relating the image onto the entrance slit of the spectrometer. The blue beam indicates the excitation beam provided by the OPO tuned to 465 nm and the green beam represents emission arising from the single cell laser sample. The lens L1 can be removed to image real-space instead of Fourier-space.

## 2.2. Optical characterization

Bright field imaging and optical excitation of individual cells inside the cavity was performed with a custom build inverted fluorescence microscope which is schematically shown for Fourier-imaging in figure 1(c). The output from an optical parametric oscillator (OPO; pulse duration, 5 ns; repetition rate, 5 Hz; tuned to 465 nm) was passed through a dichroic beam splitter (DBS; cut-on wavelength, 500 nm) and focussed into the cavity with a 40 $\times$  microscope objective. The longer wavelength emission was collected through the same objective and directed into a collection path by the DBS. For bright field imaging or to simply image the emission of a single cell laser, light was passed through a projection lens and directed toward a CCD camera via a flip mirror (beam path not shown in figure 1(c)). To record the emission spectrum of the laser or perform real-space emission measurements (hyperspectral imaging), the lens L1 (see figure 1(c)) was removed and the cavity emission collected by the objective was focused onto the entrance slit of a spectrometer equipped with a CCD array detector using a projection lens (L2). For hyperspectral imaging the entrance slit of the spectrometer was fully opened to form an image of the near field emission pattern on

the CCD array detector while at the same time decomposing the emission into the different wavelength components. This allows to study the spectral position of lasing modes without losing information about the mode pattern and nature. A more detailed description of the hyperspectral imaging technique can be found in [5]. For Fourier emission studies, the excitation path remained unchanged but an additional lens was introduced into the collection path (lens L1 in figure 1(c)) to image the back-focal plane of the objective onto the entrance slit of the spectrometer. This configuration allowed investigating the angle-dependent emission of the cavity [22]. To perform pump energy dependent measurements and record input–output characteristics of single cell lasers, the OPO output was passed through a pair of polarizers with the angle between the first polarizer and the polarization of the OPO emission adjusted by a computer controlled stepper motor to adjust the pump pulse energy. Emission spectra were again collected on the CCD array detector and integrated to determine the total single cell laser output.

## 2.3. Fluorescent microsphere laser

In order to compare the emission properties of the single cell laser to an idealized situation, we replaced the fluorescent cells with fluorescent microspheres consisting of polystyrene divinylbenzene (PS-DVB, Fisher Scientific). According to the manufacturer, the spheres had a refractive index of  $n = 1.60$  and an average diameter of 15  $\mu\text{m}$ . Optical gain was provided by internal staining of the microspheres with a proprietary fluorescent dye (Firefli Green,  $\lambda_{\text{max}} = 510 \text{ nm}$ ). The microspheres were suspended in immersion oil ( $n = 1.51$ ) and delivered into a Fabry–Pérot cavity similar to the one used with cells, but using 20  $\mu\text{m}$  glass beads for setting the cavity length.

## 2.4. Fluorescent dye laser

As a further reference, we also investigated a cavity solely filled with a fluid gain medium. With this configuration it is possible to study the case for simple 1D photonic confinement and to compare this to the emission provided by a structure with a certain refractive index landscape. The gain fluid consisted of an aqueous solution of the fluorescent dye Pyrromethene 556 (PM556, Disodium-1,3,5,7,8-pentamethylpyrromethene-2,6-disulfonate-difluoro-borate, Exciton Inc.). A concentration of 5  $\text{mmol l}^{-1}$  was dissolved in deionized water and transferred into a cavity with 10  $\mu\text{m}$  spacing by capillary forces. The refractive index of the dye solution  $n = 1.342 \pm 0.015$  was obtained by measuring the angle dependent dye emission from a distributed feedback grating [23].

## 3. Results and discussion

### 3.1. Basic laser characteristics

The basic characterization of extracellular lasers and hyperspectral imaging of their emission has been described earlier [5, 14, 15, 24]. For completeness and context, we briefly summarize the characteristics of the CMFDA based single cell

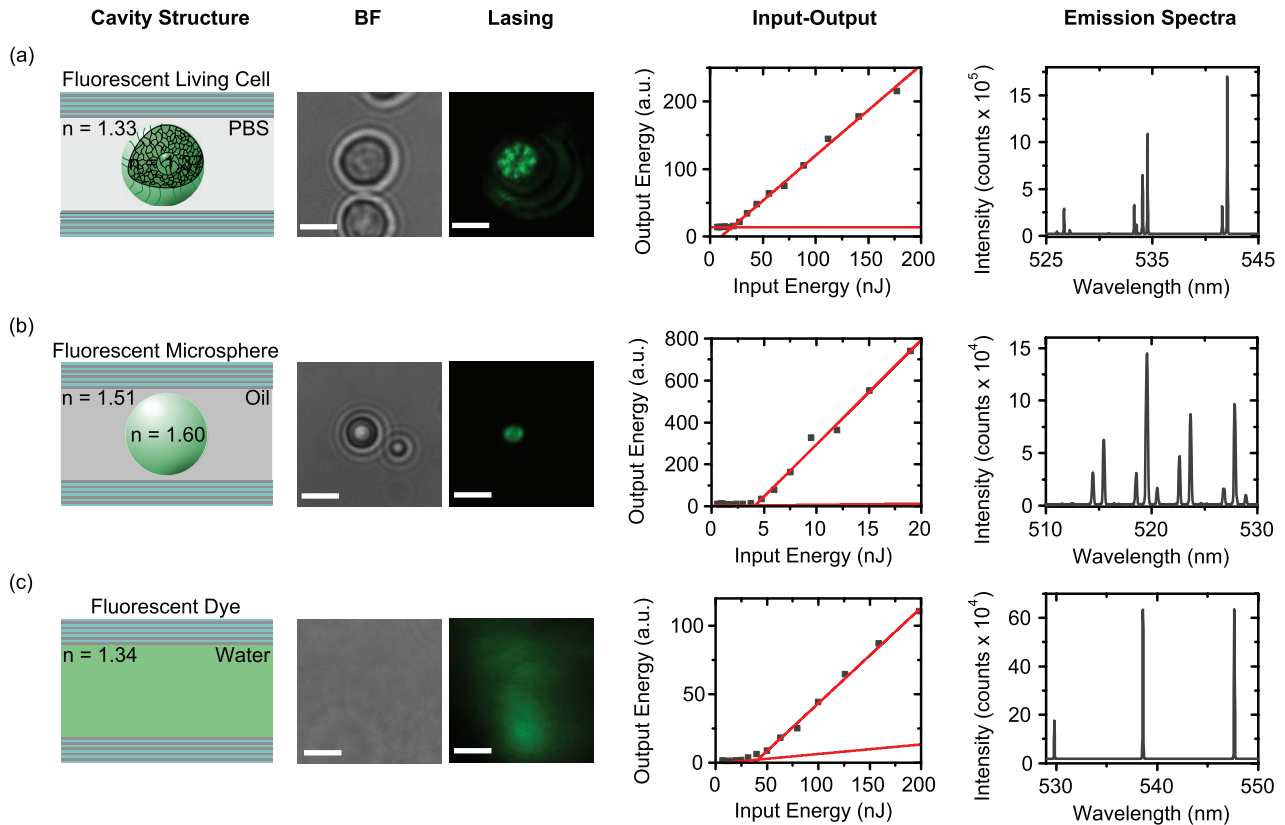


**Figure 2.** Basic characterisation of three different microcavity structures based on (a) a fluorescent living cell suspended in PBS (phosphate buffered saline solution), (b) a fluorescent microsphere suspended in immersion oil and (c) a solution of fluorescent dye without refractive index contrast. Shown are an illustration of the different cavity structures, a representative bright field (BF) image and an image of the near field laser emission (scale bars, 20  $\mu\text{m}$ ). Also shown are the input–output characteristics for each cavity structure (red lines, linear fits to data below and above threshold) and an emission spectrum above the lasing threshold.

lasers investigated here. Figure 2(a) shows an illustration of the single cell laser, a typical bright field image of cells within the cavity and a representative near field emission image of a lasing cell. The latter shows a complex pattern which was previously found to result from the overlay of several simultaneously lasing longitudinal and transverse cavity modes. Figure 2(a) also shows the input–output characteristics for the same cell, indicating that the onset of lasing occurs at a threshold pump pulse energy of 25 nJ. Finally, the associated emission spectrum of the single cell laser above threshold is also shown. The spectrum is composed of three groups of sharp peaks and these have previously been found to be associated with lasing from different longitudinal and transverse cavity modes (see below) [5].

As a simple model for a single cell laser, we also investigated Fabry–Pérot cavities containing polystyrene microspheres with diameters similar to typical cells that are doped with a green fluorescent dye (figure 2(b)). These microspheres show lasing even in the absence of a Fabry–Pérot cavity, at least when present in air or immersed in water [11]. This is a result of the substantial refractive index contrast between polystyrene and air ( $\Delta n \approx 0.6$ ) or water ( $\Delta n \approx 0.27$ ), which leads to the formation of whispering gallery modes within the microspheres. This situation is not desirable for the purpose of mimicking an extracellular laser where the refractive index contrast between cell and the surrounding cell culture

medium or PBS is ( $\Delta n \approx 0.04$ ). Therefore a high refractive index immersion oil was used instead of aqueous PBS to disperse the microspheres. This resulted in an estimated refractive index contrast of ( $\Delta n \approx 0.09$ ). A bright field image and the near field emission pattern of a typical fluorescent microsphere (diameter, 12.54  $\mu\text{m}$ ) within the cavity under lasing conditions are shown in figure 2(b). The input–output characteristics of this structure reveal a lasing threshold of 4 nJ, considerably lower than the single cell laser. We attribute this to a combination of the higher concentration of dye molecules in the microspheres, reduced intracavity light scattering and the slightly higher  $\Delta n$  which results in an increased lensing effect compared to the single cell laser. The use of a different dye and the longer cavity may also contribute to the difference in threshold. As before, the emission spectrum consists of multiple peaks as expected for a Fabry–Pérot cavity. These peaks are also clustered in groups, which we will show below are associated with emission from several transverse modes for each longitudinal laser mode. The spectral separation between these groups, i.e. the FSR of the laser cavity, is  $\Delta\lambda_{\text{FSR}} = (4.1 \pm 0.2)$  nm which corresponds to a cavity length of  $l_c = \lambda_0^2/2n_c\Delta\lambda_{\text{FSR}} = (20.5 \pm 1.6)$   $\mu\text{m}$ , consistent with the 20  $\mu\text{m}$  diameter spacer beads used. Here,  $l_c$  is the geometrical cavity length,  $\lambda_0$  the vacuum wavelength and  $n_c$  the average intracavity refractive index.

In order to compare the emission properties of the fluorescent cell and microsphere lasers to a case without in-plane refractive index contrast, we also investigated a simple cavity filled with a dye solution (figure 2(c)). Compared to the other two cases, the near field emission originates from a larger area which we attribute to the dye being present across the entire size of the pump spot (pump spot diameter,  $\approx 15 \mu\text{m}$ ) and to the absence of confinement in plane. The lasing threshold is higher than for both structures with photonic confinement (50 nJ). As before, a series of sharp peaks appears in the emission spectrum above the lasing threshold but now these occur as individual peaks and not in groups. The FSR of  $\Delta\lambda_{\text{FSR}} = (9.1 \pm 0.2) \text{ nm}$  corresponds to a cavity length of  $l_c = (11.5 \pm 0.9) \mu\text{m}$ , consistent with the  $10 \mu\text{m}$  spacer beads used to separate the mirrors.

### 3.2. Characterization of cell induced optical confinement

Next, to study the cavity physics of single cell lasers and to explore the 3D refractive index landscapes they form in more detail, we combined hyperspectral- and Fourier-imaging techniques and related the real space emission of our microcavity structures to the emission in momentum space.

For a simple Fabry–Pérot microcavity, standing waves occur at normal incidence if the optical length of the cavity  $l_{nc}$  is an integer multiple (longitudinal mode number,  $m$ ) of half the wavelength of the emitted light ( $\lambda_c$ )

$$l_{nc} = m \frac{\lambda_c}{2}; \quad m \in \mathbb{N}. \quad (1)$$

Due to energy and momentum conservation, photons within the microcavity can only attain a specific  $\mathbf{k}$ -vector that is determined by the general dispersion relation

$$E = \hbar c |\mathbf{k}| = \hbar c \sqrt{k_z^2 + k_x^2 + k_y^2}, \quad (2)$$

where  $E$  is the photon energy,  $\hbar$  the reduced Planck constant,  $c$  the speed of light and  $k_i$  the projection of the  $\mathbf{k}$ -vector into the  $i$ -direction (with  $i = x, y, z$ ).

Figure 3 shows the Fourier-space emission and the real-space emission for the three different cavity configurations. For the microcavity filled just with fluorescent dye solution (figure 3(c)), the Fourier image clearly shows the parabolic cavity mode which originates from the 1D photonic confinement between the mirrors ( $z$ -direction) with no confinement in the  $x$ - $y$ -plane (i.e.  $k_x$  and  $k_y$  can take arbitrary values). Taking into account the angle dependence of the wavevector  $|\mathbf{k}| = k_z / \cos \theta \approx (2\pi/\lambda_c)(1 + \theta^2/2)$  for small  $\theta$ , with  $\theta$  being the angle to the normal of the cavity plane, one can rewrite equation (2)

$$E \approx \hbar c \frac{m\pi}{l_{nc}} \left( 1 + \frac{\theta^2}{2} \right). \quad (3)$$

Fitting equation (3) to the measured data yields a cavity mode (white dashed line in figure 3(c)) with a longitudinal mode number  $m = 73$ . As expected, the laser emission is from the lowest energy point of the parabolic cavity mode, i.e. at  $\theta = 0^\circ$ . However, in addition to the main emission at  $\theta = 0^\circ$ ,

some laser emission is scattered towards larger angles, into the cavity dispersion profiles of different lower order longitudinal modes. Figure 3(c) also shows the real-space emission of the same cavity revealing a Gaussian like emission spot that resembles the profile of the pump spot. In addition there is some unstructured in-plane scattering away from the main lasing peak which we attribute to a combination of surface roughness of the mirrors and residual tilt of the laser mirrors which in the absence of confinement can lead to beam walk-off [15].

When placing a fluorescent cell surrounded by PBS into the microcavity, the emission in Fourier- and real-space changes drastically (figure 3(a)). In the Fourier domain there are now a number of prominent and distinct lasing states. The red dashed line in the Fourier image in figure 3(a) marks the parabolic cavity mode (longitudinal mode number  $m = 97$ ) of an unstructured microcavity with an intracavity refractive index equal to the refractive index encountered by a mode propagating through a cell. The refractive index contrast in the  $x$ - $y$ -plane that is introduced by the refractive index of the cell being larger than the index of the surrounding medium means that  $k_x$  and  $k_y$  can only take a discrete set of values. Therefore, equation (1) no longer predicts a continuous parabolic dispersion relation, but a series of discrete modes which are blue shifted in energy compared to the ground state energy of the corresponding parabolic cavity mode.

There is also a faint trace of the parabolic dispersion of the bare cavity mode (i.e. with intracavity refractive index of the medium surrounding the cell, white dashed line, longitudinal mode number  $m = 93$ ) which we attribute to photons scattered into the pure cavity mode by intracellular structures. As with the laser emission from the fluorescent dye cavity (see figure 3(c)), the lasing modes again scatter into lower order cavity modes at larger angles.

The real-space measurement of the same single cell laser (figure 3(a), real-space) shows that lasing is not just from different longitudinal modes but split into several transverse modes. The transverse mode patterns are elliptical in shape and of Ince–Gaussian nature. Ince–Gaussian modes (IGMs) are generalized orthogonal paraxial modes in elliptic coordinates, and describe the transition between spherical Laguerre–Gaussian modes (LGMs) with circular symmetry and Hermite–Gaussian modes (HGMs) with rectangular symmetry. We attribute the origin of the Ince–Gaussian modes to a slightly elliptical shape of the cells. Modes with mode indices from  $(0, 0)_{97}$  to  $(2, 0)_{97}$  are observed (here the transverse mode numbers  $p$  and  $q$  and the longitudinal mode number  $m$  are given as  $(p, q)_m$ ). We observe a small energetic difference between the  $(2, 0)_{97}$  and the  $(0, 2)_{97}$  mode which is also most likely a result of the slightly elliptical shape of the cell.

The energetic states of the single cell laser in Fourier-space can be directly related to transverse mode patterns observed in real-space. As expected, the spectral position and the number of nodes for each mode is identical in Fourier- and real-space. For example, the  $(0, 0)_{97}$  Ince–Gaussian mode (IGM) in real-space corresponds to a single peak of constant energy in Fourier-space whereas the  $(1, 0)_{97}$  IGM

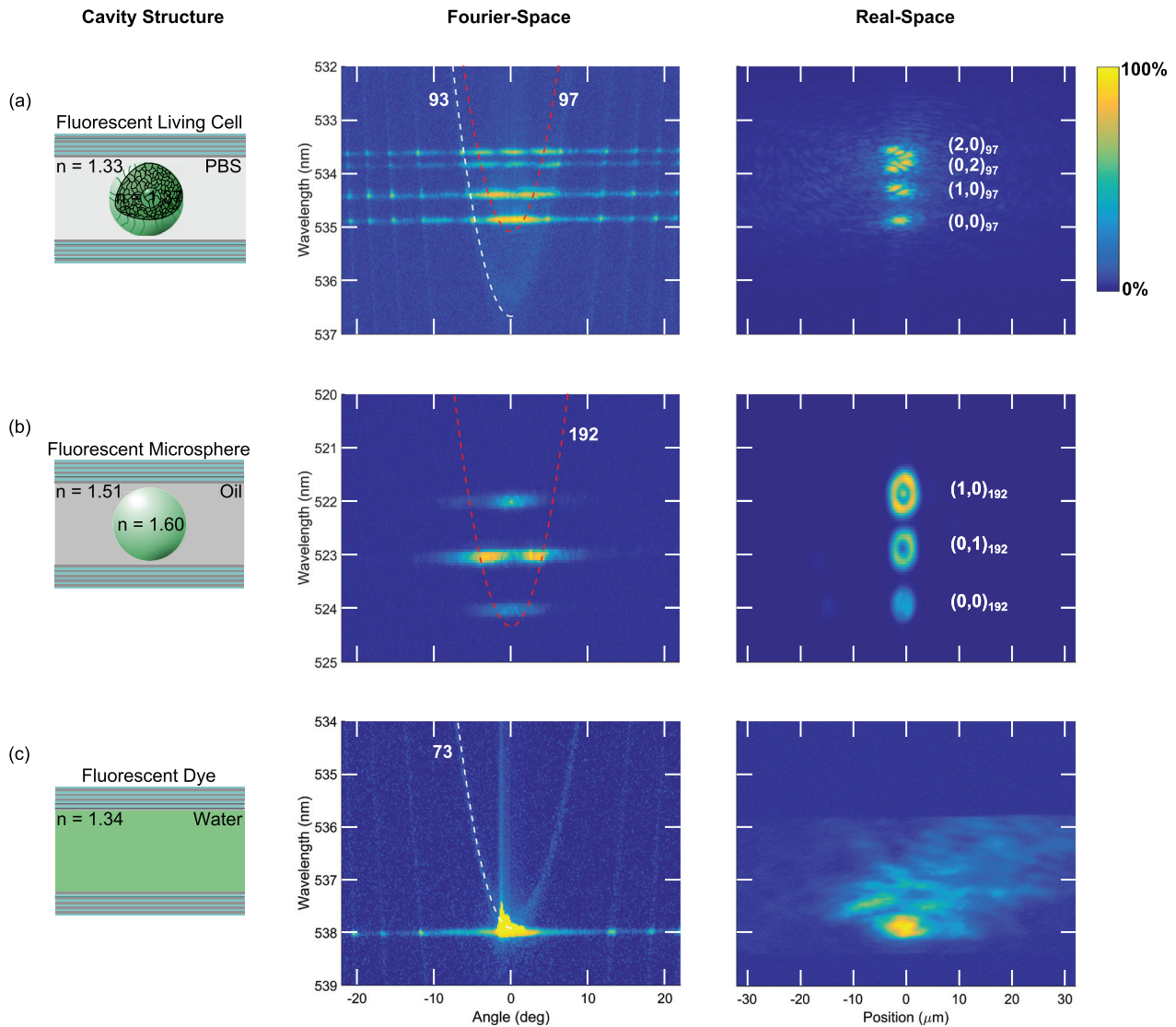


**Figure 3.** Fourier-space and real-space characterization of lasing from the cell based cavity and from the two reference cavity structures. The Fourier-space images show a heatmap of the laser emission from the cavity as a function of wavelength and angle. White dashed lines indicate the bare cavity mode (assuming an intracavity refractive index of water); red dashed lines indicate the cavity mode for the average refractive index encountered by a mode propagating through a cell and a polystyrene microsphere, respectively. Numbers indicate the corresponding longitudinal mode number  $m$ . The real-space images show the spatially and wavelength resolved emission of the different laser modes. For the cell and the polystyrene sphere, the transverse mode numbers  $p$  and  $q$  and the longitudinal mode number  $m$  are given next to each mode as  $(p, q)_m$ .

in real-space corresponds to two peaks of constant energy in Fourier-space, etc.

As a control measurement and to mimic an ideal single cell laser without scattering and with near-perfect sphericity, we also measured the emission from the cavity structure based on a fluorescent polystyrene microsphere in immersion oil (figure 3(b)). The pattern observed in Fourier-space resembles the single cell laser, but the bare cavity mode is absent. We attribute this to a combination of much weaker internal scattering and slightly stronger photonic confinement introduced by the polystyrene microsphere. In the real-space emission of the fluorescent microsphere laser, the first three fundamental LGMs can be identified. (LGMs rather than IGMs are observed due to the more spherical shape of the microsphere compared to the cell.) As for the single cell laser, the energetic

states in Fourier-space can be directly related to the transverse mode pattern in real-space.

### 3.3. Comparison of real- and Fourier-space emission of single cell laser

Compared to microcavity studies performed on light-emitting inorganic or organic semiconductors, predicting the specific modes supported and created by cell-based photonic structures is more challenging. This is due to their larger variability in size and shape. However, the unique transverse mode pattern of single cell lasers may allow one to distinguish different cells from each other.

Figure 4 shows a selection of transverse lasing mode patterns for a number of different cells, directly comparing

Fourier- and real-space data for each case. For each example, the number of nodes seen in the real-space IGM pattern is the same as the number of nodes of the energetic states in Fourier-space.

The data also show that while even higher order modes (e.g. the (6, 0) mode) remain spatially confined to the cell boundary in real-space, their higher energy state position within the cell cavity means they are emitted less directionally, i.e. into a larger range of angles. For example, even though the cell sizes are comparable, the (6, 0) mode emission has a divergence of  $\Delta\theta = (21 \pm 1)^\circ$  whereas the divergence of the (0, 0) mode emission is only  $\Delta\theta = (5 \pm 1)^\circ$ .

In the hyperspectral images (real-space emission) it can be seen that the extent of transverse modes is clearly confined to the boundary between cell and surrounding medium, even for higher mode numbers. For example, the two outer emission peaks (left and right) for mode (3,0) follow the slightly elliptical shape of the cell.

### 3.4. Input–output characteristics in Fourier-space

We further investigated the lasing threshold for states/modes with different energies and momenta. Figure 5(a) shows the Fourier-space emission of a single cell laser operating at the longitudinal mode numbers  $m = 112$  and  $m = 111$ . As before in figure 3(a), we also show the parabolic dispersion relation of an unstructured cavity with an intracavity refractive index corresponding to the average refractive index encountered by a mode propagating through the cell (red dashed line).

The threshold behaviour of this laser was investigated separately for four different energy and momentum states by integrating the intensity over the respective regions on the CCD detector attached to the spectrograph. The highest energy emission state of these four states (labelled  $(p, q)_{112}$  in figure 5(a)) occurs at an emission wavelength of  $(540.6 \pm 0.2)$  nm. From the corresponding input–output characteristics (black symbols, upper panel in figure 5(b)), we derive a lasing threshold of 25 nJ for this mode (threshold indicated as T1 in figure 5(b)). Similar input–output characteristics and lasing threshold are observed for a mode with the same transverse mode pattern but a lower longitudinal mode number (see  $(p, q)_{111}$  in figure 5(a) and red symbols in upper panel of figure 5(b)). We attribute this to the fact that the wavelengths of both modes are very close to the emission maximum of the intracellular gain material and that both have the same spatial profile which means that the overlap of the mode with the gain medium and with any scattering or absorbing structures in the cell is very similar.

The mode appearing close to the low-energy end of the parabolic cavity dispersion is the fundamental  $(0, 0)_{112}$  mode. The input–output characteristics for this mode are shown as blue symbols in figure 5(b), central panel. Compared to the higher order transverse mode  $(p, q)_{112}$ , the lasing threshold is more than three-times higher (89 nJ, indicated by T2 in figure 5(b)). Therefore, in a single cell laser—as opposed to precisely fabricated inorganic VSCSEL [25]—the most favourable lasing mode is not necessarily the fundamental (lowest order) transverse mode but can be of higher transverse order.



**Figure 4.** Different Ince–Gaussian transverse modes emitted by single cell lasers imaged in Fourier-space (*F*) and real-space (*R*). The modes are from different cells and ordered according to the transverse mode number, from (0, 0) to (6, 0). The cell boundary of the corresponding cells is highlighted by a white line in each real-space emission image. The scale is given in  $\mu\text{m} \times \mu\text{m}$  for the real-space emission images and in  $\text{nm} \times \text{degree angle}$  for the Fourier-space emission images.

This suggests the 3D refractive index and gain profile defined by the cell provides higher modal gain to a mode with a more complex structure and larger spatial extent.

We also analysed the influence of the momentum position on the lasing threshold by comparing emission from the high order transverse mode  $(p, q)_{112}$  that is emitted at  $0^\circ$  to emission at the same wavelength but at higher angles (labelled  $(p, q)_{112}^*$  in figure 5(a)). The corresponding input–output characteristics (figure 5(b), lower panel) show that emission from the higher momentum state  $(p, q)_{112}^*$  was considerably weaker than from the centre state  $(p, q)_{112}$ . However, the onset for lasing is at the same pump pulse energy for both states. We take this as evidence that both features are due to the same mode and that in this cavity structure, emission at larger momentum results from scattering of lower momentum transverse modes with the same wavelength. The scattering process is linear and so the measured thresholds of all momentum states with identical wavelength/energy are the same, independent of their emission angle. This behaviour is different from our earlier

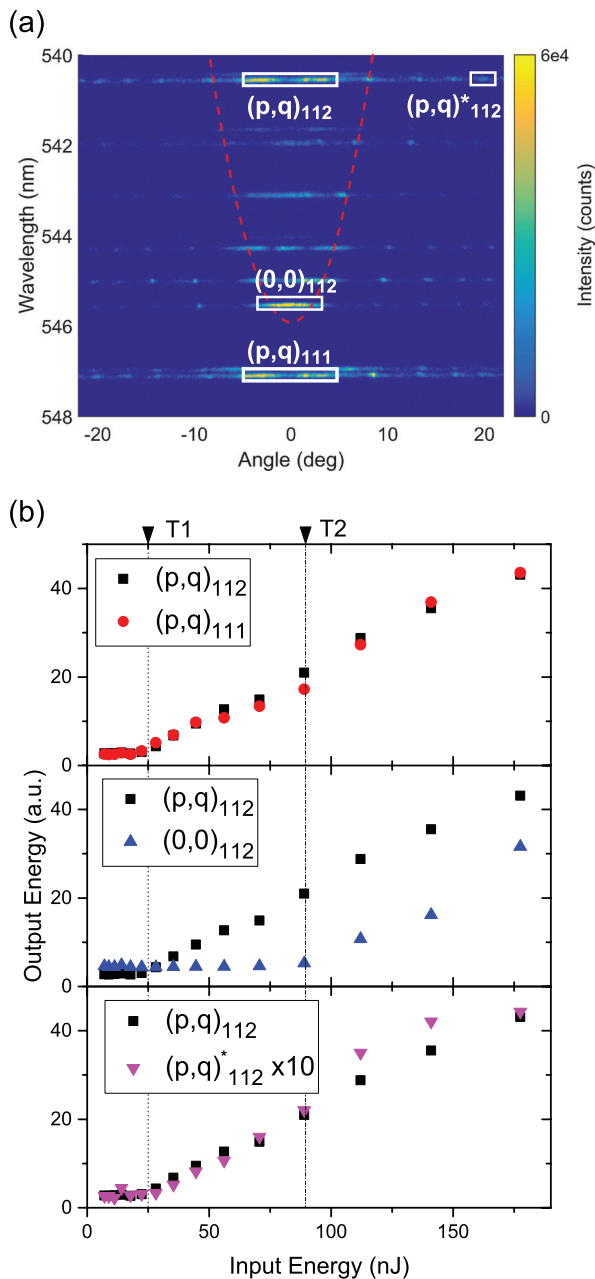


**Figure 5.** Input–output characteristics of a single cell laser at different energy and momentum positions, i.e. different lasing states/modes. (a) Fourier-space image of the laser emission, showing the four emission states investigated (areas marked by white boxes and labelled with the respective mode number). Also shown is the expected dispersion for an unstructured cavity with an intracavity refractive index corresponding to the effective refractive index encountered by the supported modes. (b) Threshold curves for the different energy and momentum states. Mode  $(p, q)_{112}$  (black symbols) is compared to a mode with different longitudinal but same transverse mode number ( $(p, q)_{111}$ , red symbols), as well as to the fundamental mode of the same longitudinal mode family ( $(0, 0)_{112}$ , blue symbols) and to the emission state of the same mode at larger angles ( $(p, q)_{112}^*$ , purple symbols, output values multiplied by 10 for better visibility).

observations in microcavities containing thin films of solid-state GFP as optical gain medium [18].

#### 4. Conclusion

Using combined Fourier- and hyperspectral imaging techniques, we showed that placing a fluorescent cell into a microcavity gives rise to a 3D photonic confinement. By comparing the single cell laser emission to the emission from a cavity filled with a fluorescent dye and to the emission from a cavity with a fluorescent polystyrene microsphere, we concluded that the photonic confinement is due to the refractive index contrast between the cell and the surrounding medium. The energetic states in Fourier-space can be related directly to the transverse mode patterns in real-space. This direct relation allows predictions of the specific longitudinal and transverse mode pattern. Comparing the Fourier- and real-space emission further revealed an increase in the divergence of the emitted laser light with transverse mode order. Investigating the input–output characteristics of a single cell laser in Fourier-space at different energy and momentum positions gave insight into how the different longitudinal and transverse lasing modes are formed. These in depth characterizations will be helpful for introducing biological single cell lasers as a tool for sensing intracellular characteristics which may lead to a cell-laser based cytometry. In addition, by shrinking resonator size and thus decreasing the effective mode volume, it may be possible to observe strong coupling and potentially low threshold polariton lasing from single cells.

#### Acknowledgments

We acknowledge financial support from the European Research Council (ERC StG ABLASE, 640012), the Scottish Funding Council (via SUPA) and the European Union Marie Curie Career Integration Grant (PCIG12-GA-2012-334407). MK acknowledges funding from the EPSRC DTG (EP/M506631/1). MS acknowledges funding from the European Commission for a Marie Skłodowska-Curie Individual Fellowship (659213). IDWS acknowledges funding from a Royal Society Wolfson research merit award. The research data supporting this publication can be accessed at <https://doi.org/10.17630/5db16bfb-7619-480d-a9b8-623eda60d020>.

#### References

- [1] Maiman T H 1960 Stimulated optical radiation in ruby *Nature* **187** 493–4
- [2] Dougherty T J, Gomer C J, Henderson B W and Peng Q 1998 Photodynamic therapy *J. Natl Cancer Inst.* **90** 889–905
- [3] Tanzi E L, Lupton J R and Alster T S 2003 Lasers in dermatology: four decades of progress *J. Am. Acad. Dermatol.* **49** 1–31

- [4] Roorda A, Romero-Borja F, Donnelly W III, Queener H, Hebert T and Campbell M 2002 Adaptive optics scanning laser ophthalmoscopy *Opt. Express* **10** 405–12
- [5] Gather M C and Yun S-H 2011 Single-cell biological lasers *Nat. Photon.* **5** 406–10
- [6] Siddique M, Yang L, Wang Q Z and Alfano R R 1995 Mirrorless laser action from optically pumped dye-treated animal tissues *Opt. Commun.* **117** 475–9
- [7] Vannahme C, Maier-Flaig F, Lemmer U and Kristensen A 2013 Single-mode biological distributed feedback laser *Lab Chip* **13** 2675–8
- [8] Camposeo A, Del Carro P, Persano L, Cyprych K, Szukalski A, Sznitko L, Mysliwiec J and Pisignano D 2014 Physically transient photonics: random versus distributed feedback lasing based on nanoimprinted DNA *ACS Nano* **8** 10893–8
- [9] Gather M C and Yun S-H 2014 Bio-optimized energy transfer in densely packed fluorescent protein enables near-maximal luminescence and solid-state lasers *Nat. Commun.* **5** 5722
- [10] Chen Y-C, Chen Q and Fan X 2016 Optofluidic chlorophyll lasers *Lab Chip* **16** 2228–35
- [11] Schubert M, Steude A, Liehm P, Kronenberg N M, Karl M, Campbell E C, Powis S J and Gather M C 2015 Lasing within live cells containing intracellular optical microresonators for barcode-type cell tagging and tracking *Nano Lett.* **15** 5647–52
- [12] Humar M and Yun S-H 2015 Intracellular microlasers *Nat. Photon.* **9** 572–6
- [13] Chalfie M and Kain S R 2005 *Green Fluorescent Protein: Properties, Applications and Protocols* (New York: Wiley) (doi: [10.1002/0471739499](https://doi.org/10.1002/0471739499))
- [14] Nizamoglu S, Lee K-B, Gather M C, Kim K S, Jeon M, Kim S, Humar M and Yun S-H 2015 A simple approach to biological single-cell lasers via intracellular dyes *Adv. Opt. Mater.* **3** 1197–200
- [15] Humar M, Gather M C and Yun S-H 2015 Cellular dye lasers: lasing thresholds and sensing in a planar resonator *Opt. Express* **23** 27865
- [16] Fan X and Yun S-H 2014 The potential of optofluidic biolasers *Nat. Methods* **11** 141–7
- [17] Vahala K J 2003 Optical microcavities *Nature* **424** 839–46
- [18] Dietrich C P, Höfling S and Gather M C 2014 Multi-state lasing in self-assembled ring-shaped green fluorescent protein microcavities *Appl. Phys. Lett.* **105** 233702
- [19] Dietrich C P, Steude A, Tropf L, Schubert M, Kronenberg N M, Ostermann K, Höfling S and Gather M C 2016 An exciton-polariton laser based on biologically produced fluorescent protein *Sci. Adv.* **2** e160666
- [20] Brückner R, Zakhidov A A, Scholz R, Sudzius M, Hintschich S I, Fröb H, Lyssenko V G and Leo K 2012 Phase-locked coherent modes in a patterned metal-organic microcavity *Nat. Photon.* **6** 322–6
- [21] Reinhardt C, Brückner R, Haase J, Sudzius M, Hintschich S I, Fröb H, Lyssenko V G and Leo K 2012 Mode discretization in an organic microcavity including a perforated silver layer *Appl. Phys. Lett.* **100** 103306
- [22] Lai C W, Kim N Y, Utsunomiya S, Roumpos G, Deng H, Fraser M D, Byrnes T, Recher P, Kumada N, Fujisawa T and Yamamoto Y 2007 Coherent zero-state and  $\pi$ -state in an exciton-polariton condensate array *Nature* **450** 529–32
- [23] Karl M, Whitworth G L, Schubert M, Dietrich C P, Samuel I D W, Turnbull G A and Gather M C 2016 Optofluidic distributed feedback lasers with evanescent pumping: reduced threshold and angular dispersion analysis *Appl. Phys. Lett.* **108** 261101
- [24] Kar A K, Mackenzie M D, Cialowicz K I, Saleeb R S and Duncan R R 2016 Vitamin C for stabilising biological lasers *Proc. SPIE* **9711** 1K
- [25] Chong C H and Sarma J 1993 Lasing mode selection in vertical-cavity surface emitting-laser diodes *IEEE Photonics Technol. Lett.* **5** 761–4